RSC Advances

PAPER

View Article Online
View Journal | View Issue

Cite this: *RSC Adv.*, 2026, **16**, 29291

Bis-thiosemicarbazone functions as a selective chemosensor with the lowest LOD for Hg ions in water-rich medium: implications for on-site detection and logic gate experiments

Sanyog Sharma, *[a] Nabajyoti Patra,[b] Navdeep Kaur,[c] Pratap Kumar Pati,[c] Sanjay Mandal,[d] P. V. Bharatam *[b] and Tarlok Singh Lobana *[a]

Received 27th March 2026
Accepted 14th May 2026

DOI: 10.1039/d6ra02561g

rsc.li/rsc-advances

In this investigation, a mesitylene-anchored bis-thiosemicarbazone (**TOMH**), with the potential to chelate a metal ion *via* S,S donor atoms, was used as a chemosensor for the selective detection of mercury ions in an aqueous medium from mixtures with several metal ions (Ag, Al, Ba, Bi, Ca, Cd, Co, Cr, Cs, Cu, Fe, K, Li, Mg, Mn, Na, Ni, Pb, Th, and Zr). Electronic absorption spectroscopy revealed the composition of the identified species to be Hg(S,S-TOMH)·$(NO_3)_2$ (**TOMHN**). The spectroscopic (^{1}H NMR, ^{13}C NMR, and FT-IR), theoretical (DFT and TD-DFT) and structural techniques confirmed the bonding of **TOMH** to Hg through S donor atoms (Hg–S: 2.484–2.490 Å and S–Hg–S bond angle: 160.1°), while the nitrates are non-bonded. The **TOMH** chemosensor has the lowest limit of detection (LOD: 10.97 nM) for Hg ions in a water-rich medium (90% H_2O : 10% DMSO) among thiosemicarbazones or closely related S donor chemosensors. It exhibits multiple applications, such as on-site detection of Hg using filter paper strips, formation of **TOMH**–Hg–EDTA-supported INHIBIT logic gate, and enhanced antimicrobial activity of **TOMHN** relative to **TOMH** or $Hg(NO_3)_2$ alone.

1 Introduction

Environmental pollution is among the most challenging issues confronting human society today. One cause of pollution is linked to the presence of heavy metals, which may threaten various living organisms owing to their toxic nature.[1] For instance, mercury, as its inorganic salts or organomercury derivatives,[2–5] disrupts protein and enzyme functions and affects the kidneys and brain.[6–15] The acceptable limit of mercury in drinking water is 10 nM as per the US Environmental Protection Agency.[16,17] The burning of fossil fuels, incineration of garbage, mining, and natural volcanic eruptions all contribute to the rise of Hg contamination.[18] Thus, in order to monitor mercury in the environment, several analytical techniques, such as chromatography, high-performance liquid chromatography (HPLC), inductively coupled plasma-mass spectrometry (ICP-MS), flow injection technologies, and atomic absorption spectroscopy (AAS), have been used.[19–28] Further, colorimetric techniques, being easily accessible due to their low cost, have played a significant role as chemosensors in the selective detection of metal ions.[29–35] Our group has used colorimetric techniques for the detection of analytes consisting of metal ions (Cu and Al), neutral molecules (picric acid) or anions (F^- and CN^-) with the help of chemosensors based on a variety of aromatic platforms containing imine/hydroxyl, hydrazone, thiourea and other functional groups.[36–44]

It is known that thiosemicarbazones, a distinct class of organic compounds, can chelate metal ions through their N,S or S donor atoms and thus serve as cost-effective chemosensing materials.[45–49] In the literature, there are several reports of mono-thiosemicarbazone-based chemosensors for detecting mercury at nanomolar levels in aqueous media. However, in these cases, the aqueous medium generally requires a higher proportion of organic solvent with higher LODs (approx. 31 to 900 nM).[50–53] There is another class of chemosensors based on pyrazole-, thiourea-, and napthothiazole-type organic compounds used for the detection of mercury, and their LODs range from 21 nM to 69.02 μM.[54–70] In these cases, it is also observed that the aqueous medium requires a higher proportion of organic solvent. Limited studies of Hg detection in water medium alone have been reported in the literature.[55,71] This survey (Table S1) prompted us to seek alternative chemosensors with the primary goal of detecting Hg at lower LODs in predominantly water-containing media. For this purpose, a bis-thiosemicarbazone (Fig. 1, **TOMH**) with multiple electron-rich

[a]*Department of Chemistry, UGC Center for Advanced Studies, Guru Nanak Dev University, Amritsar 143005, Punjab, India. E-mail: sharma.sanyog@yahoo.com; tarlokslobana@yahoo.co.in*

[b]*Department of Medicinal Chemistry, National Institute of Pharmaceutical Education and Research, S. A. S. Nagar 160062, Punjab, India. E-mail: pvbharatam@niper.ac.in*

[c]*Department of Biotechnology, Guru Nanak Dev University, Amritsar 143005, Punjab, India*

[d]*Department of Chemical Sciences, Indian Institute of Science Education and Research Mohali, S. A. S. Nagar, 140306, Punjab, India*

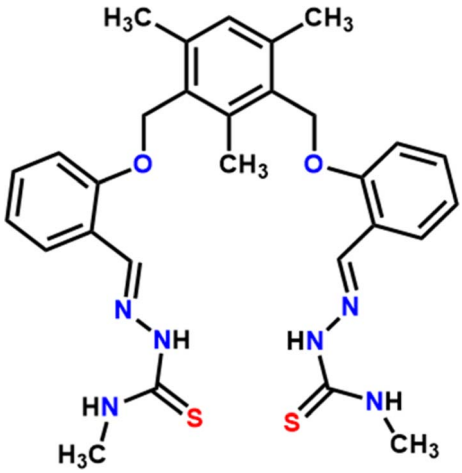

Fig. 1 2D structure of TOMH.

donor centers and two arms positioned in *cis*-orientation was selected for the present studies.

In this investigation, **TOMH** is utilized to detect Hg(II) ions in aqueous medium, and the studies include stoichiometry, bonding modes, and structural aspects of the detected species, characterized through electron absorption spectroscopy, NMR spectroscopy, theoretical techniques (DFT, TD-DFT), and crystallography. The findings indicate successful detection of Hg at the nano level in predominantly water medium, on-site Hg detection using sensor-coated paper strips, and enhanced antimicrobial activity of the detected species (Hg(S,S-TOMH)·$(NO_3)_2$) compared to that of **TOMH** or Hg salt alone.

2 Experimental section

2.1. Materials and techniques

All the commercially available chemicals were purchased from Aldrich and used without further purification. Standard methods were used to dry all of the solvents. TLC was carried out on glass sheets pre-coated with silica gel. The ^{1}H and ^{13}C NMR spectra were carried out in DMSO-d_6 with TMS as an internal reference on a Bruker Topspin-FTNMR-500 MHz spectrometer. The infrared spectra (KBr pellet) were recorded using a PerkinElmer FT-IR C92035 spectrophotometer in the range 400–4000 cm^{-1}. An SDFCL digital pH meter was used to measure the pH of the solutions. The electronic absorption spectra were recorded on a Shimadzu Pharmaspec UV-1900 UV-Vis spectrophotometer with a quartz cuvette (path length 1 cm). The absorption spectra were recorded between 1100 and 200 nm. The cell holder of the spectrophotometer was thermostatic at 25 °C for consistency in the recordings. Microwave reactions were carried out using the Anton-Par Monowave 200 microwave synthesis reactor operating at 200 W.

2.2. Synthetic procedures

2.2.1. Synthesis of (2*Z*,2′*Z*)-2,2′-(((((2,4,6-trimethyl-1,3-phenylene) bis(methylene))bis(oxy))bis(2,1-phenylene))bis(methaneylylidene))bis(*N*-methylhydrazine-1-carbothioamide) (TOMH) (Scheme S1). A previously documented method[42,72] was modified to synthesize **TOMH** to improve yield and reduce reaction time. A mixture of 0.0108 g (1.027 mmol) of 3-methylthiosemicarbazide and 0.2 g (0.5152 mmol) of aldehyde (2,2′-(((2,4,6-trimethyl-1,3-phenylene)bis-(methylene))bis(oxy)) dibenzaldehyde) suspended in 7 mL of ethanol was placed in a microwave vial and irradiated for ten minutes. After filtration and multiple washings with ethanol, the precipitate was vacuum dried for an hour. Yield: 0.280 g (97%). The product is a very pale yellow solid with a melting point of 150–152 °C (Fig. S1–S6).

2.2.2. Synthesis of $Hg(NO_3)_2$(TOMH) complex (TOMHN). A 10 mL solution of $Hg(NO_3)_2$ (0.746 g, 2.30 mmol) in methanol was added as a suspension to a 10 mL solution of **TOMH** (0.647 g, 1.15 mmol) in dichloromethane. The mixture was then refluxed for an hour. The reaction mixture was stirred for eight hours and then concentrated. Pale yellow precipitates were collected on a Buchner funnel. These precipitates were recrystallized from a mixture of CH_2Cl_2, EtOH, and CH_3CN. Yield: 0.853 g (82%). The product is a very pale yellow solid with a melting point of 188–190 °C. IR (KBr, cm^{-1}) 3202, 2919, 2838, 1596, 1445, 1300, 1233, 1156, 1111, 1073, 1026, 987, 845, 749, 562; ^{1}H NMR (500 MHz, DMSO-d_6) (δ): 2.29 (t, 3H, –CH_3, J = 10.0), 2.34 (s, 6H, –CH_3), 3.05 (s, 6H, –CH_3), 5.16 (s, 4H, –CH_2), 6.96 (s, 1H, –Ar), 7.02 (s, 2H, –Ar), 7.08 (t, 2H, –Ar, J = 10.0), 7.37 (m, 2H, –Ar), 7.55 (t, 2H, –Ar, J = 10.0), 8.09 (d, 2H, J = 5), 8.39 (s, 2H, –CH=N), 9.39 (s, 2H, –NH), 11.76 (s, 2H, –NH); ^{13}C NMR (500 MHz, DMSO-d_6) (δ): 15.45 (–CH_3), 19.83 (–CH_3), 32.06 (–N–CH_3), 65.65 (–CH_2), 113.45 (–Ar), 121.27 (–Ar), 122.20 (–Ar), 126.88 (–Ar), 130.41 (–Ar), 131.31 (–Ar), 132.71 (–Ar), 138.82 (–CH=N), 139.68 (–Ar), 141.93 (–Ar), 158.33 (–C–O), 173.42 (–C=S) (Fig. S7–S11).

2.2.3. Synthesis of HgI_2(TOMH) (TOMHI). A 10 mL solution of HgI_2 (1.0451 g, 2.30 mmol) in MeOH was added slowly to a 10 mL solution of **TOMH** (0.647 g, 1.15 mmol) in CH_2Cl_2, followed by refluxing for an hour. The reaction mixture was stirred overnight and allowed to evaporate. Pale yellow precipitates were collected on a Buchner funnel. These precipitates were recrystallized from a mixture of CH_2Cl_2, EtOH, and CH_3CN and formed fine crystals. Yield: 0.821 g (70%). The product is a white solid with a melting point of 193–195 °C. IR (KBr, cm^{-1}) 3287, 3207, 2914, 1572, 1238, 1087, 992, 855, 751; ^{1}H NMR (500 MHz, DMSO-d_6) (δ): 2.31 (s, 3H, –CH_3), 2.34 (s, 6H, –CH_3), 3.07 (d, 6H, –CH_3, J = 4.2), 5.15 (s, 4H, –CH_2), 7.04 (m, 2H, –Ar), 7.37 (d, 2H, –Ar, J = 5.0), 7.49 (t, 2H, –Ar, J = 5.0), 8.11 (d, 2H, J = 10.0), 8.38 (s, 2H, –CH=N), 8.99 (s, 2H, –NH), 11.54 (s, 2H, –NH); ^{13}C NMR (500 MHz, DMSO-d_6) (δ): 15.34 (–CH_3), 19.77 (–CH_3), 31.98 (–N–CH_3), 65.71 (–CH_2), 113.54 (–Ar), 121.11 (–Ar), 122.20 (–Ar), 126.84 (–Ar), 130.62 (–Ar), 131.27 (–Ar), 132.67 (–Ar), 134.29 (–Ar), 138.75 (–CH=N), 139.65 (–Ar), 158.31 (–C–O), 174.25 (–C=S) (Fig. S12–S15).

2.3. Spectral analysis of TOMH using UV-vis studies

A stock solution of **TOMH** (1 mM) was prepared in DMSO solvent. Similarly, stock solutions of various metal ions (also 1 mM), including Ag(I), Al(III), Ba(II), Bi(III), Ca(II), Cd(II), Co(II),

Cu(II), Cr(III), Fe(III), Hg(II), K(I), Mg(II), Mn(III), Ni(II), Na(I), Pb(II), Zn(II), *etc.*, were prepared by dissolving the corresponding salts in double-distilled water. The interaction of **TOMH** with these metal ions was investigated using UV-vis spectroscopy in 10^{-5} M solutions in DMSO.

2.4. X-ray crystallography

The crystals of the complex HgI_2(TOMH) (MF: $C_{33}H_{37}HgI_2N_8O_2S_2$) were grown by slow evaporation from a mixture of dichloromethane, acetonitrile, and ethanol. A suitable crystal was selected and mounted on a Bruker APEX4 diffractometer. The crystal was maintained at 296.15 K during data collection. Using Olex2,[73] the structure was solved with the SHELXT[74] structure solution program utilizing Intrinsic Phasing and refined with the SHELXL refinement package using least squares minimization.

2.5. Computational methodology

The 3D structures of the **TOMH** ligand and its complexes, **TOMHN** (nitrate complex) and **TOMHI** (iodide complex) were optimized in gas phase followed by frequency analysis of the same at the B3LYP/gen level of quantum theory. All calculations were carried out using the Gaussian16 suite of programs.[75–79] C, H, N, S, and O atoms were optimized using a 6-311++G(d,p) basis set, and the def-2tzvpp basis set with the effective core potential (ECP) function was used to optimize heavier atoms Hg and I. TD-DFT was carried out to predict the UV-Vis energy spectra of the **TOMH** and **TOMHN** complexes using the B3LYP/6-311++G(d,p)/def-2tzvpp method. The energies of the highest occupied molecular orbital (HOMO, ΔE_H), lowest unoccupied molecular orbital (LUMO, ΔE_L), and their associated HOMO–LUMO gap (ΔE_{H-L}) were estimated using the same basis set. Chemical descriptors such as chemical potential (μ), electronegativity (χ), hardness (η), softness (S), and electrophilicity (ω) were estimated for electronic transitions between ligand **TOMH** and associated complexes (**TOMHN** and **TOMHI**) as seen in Schemes S2–S6.[80–84] The molecular electrostatic potentials (MEP) of **TOMH**, **TOMHN**, and **TOMHI** were generated using the iop (6/7 = 3) function, and Frontier molecular orbital (FMO) diagrams of **TOMH**, **TOMHN** and **TOMHI** were obtained in implicit solvent (IEFPCM, DMSO and H_2O) model.

2.6. Antimicrobial activity

The antimicrobial activity[85–88] of the $Hg(NO_3)_2 \cdot$(TOMH) complex was evaluated against two Gram-negative (*E. coli* and *P. syringae*) and two Gram-positive bacteria (*B. subtilis* and *S. aureus*). An inoculum of 100 μL of bacterial suspension (~1×10^6 CFU mL^{-1}) was inoculated into 2 mL of Luria-Bertani (LB) broth, followed by the addition of **TOMHN** (5 μM), **TOMH** (5 μM), and

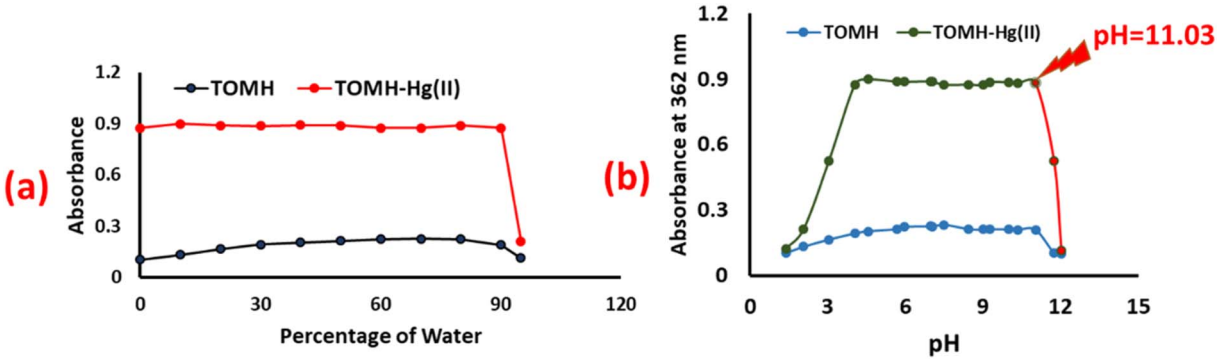

Fig. 2 Effect of (a) water fraction and (b) pH on the absorbance of **TOMH** and its solution with $Hg(NO_3)_2$ at 372 nm.

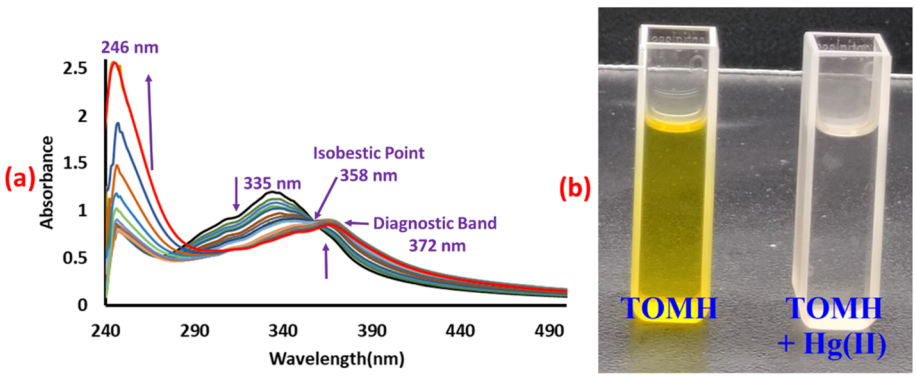

Fig. 3 (a) Changes in the absorbance spectrum of **TOMH** in DMSO : HEPES (1 : 9) (10 μM) upon the gradual addition of Hg(II). (b) Color changes in the sensor solution with Hg(II) under a UV lamp.

$Hg(NO_3)_2$ (5 μM). The cultures were incubated overnight under specific conditions: 37 °C for *E. coli* and *S. aureus*, 30 °C for *B. subtilis*, and 28 °C for *P. syringae*. Kanamycin (1 mg mL^{-1}) was taken as the reference antibiotic for the study. The optical density (OD) was measured at 600 nm, and antimicrobial activity was calculated using the following formula:

$$\text{Growth inhibition}(\%) = \frac{A_{\text{control}} - A_{\text{sample}}}{A_{\text{control}}} \times 100.$$

All experiments were performed in triplicate, and results are presented as mean ± standard error. Statistical significance was analyzed using one-way ANOVA, with a significance threshold of $p < 0.05$.

3 Results and discussion

In this section, the interaction of **TOMH** with mercury salt is described. The discussion covers (a) a variety of photophysical properties, including the effects of pH, water content, selectivity towards Hg(II), interference from other metal ions under study, stoichiometry of interaction, stability constant, detection limit, and reversible nature of the sensor, and (b) spectroscopic, structural, and computational studies.

3.1. Photophysical studies of TOMH–Hg interaction

To develop a versatile sensor, the tolerance of **TOMH** towards water and the effect of water on its detection efficiency for Hg(II) ions in a $Hg(NO_3)_2$ solution were examined. Titration

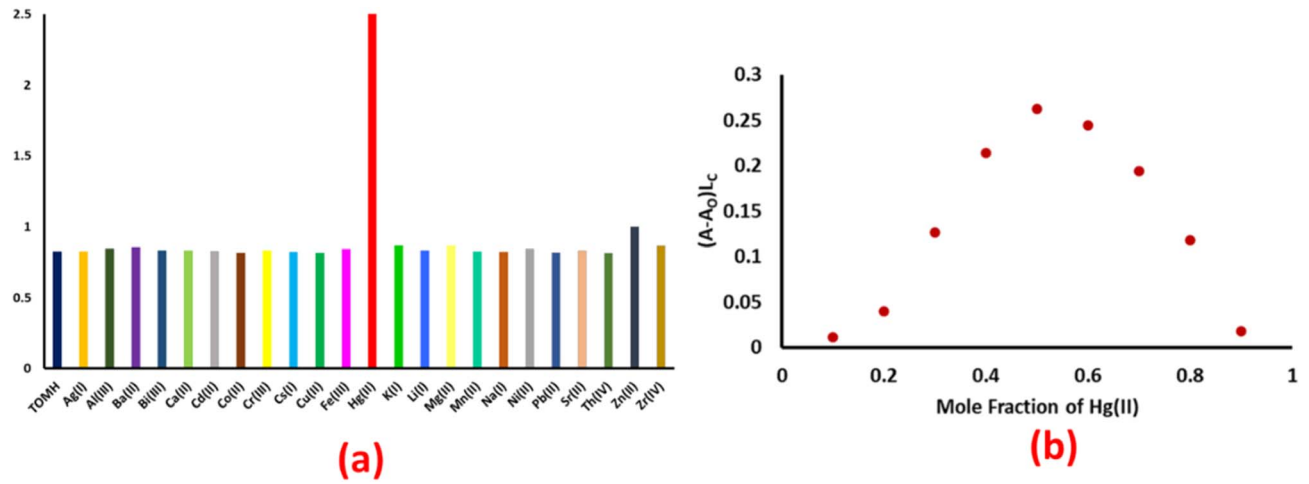

Fig. 4 (a) Effect of the addition of different metal ions (100 μM) on the spectral changes at $\lambda_{max} = 246$ nm of **TOMH** (10 μM) in a HEPES buffer (pH 7.4, containing 10% DMSO as a co-solvent). (b) Job's plot of **TOMH** with $Hg(NO_3)_2$.

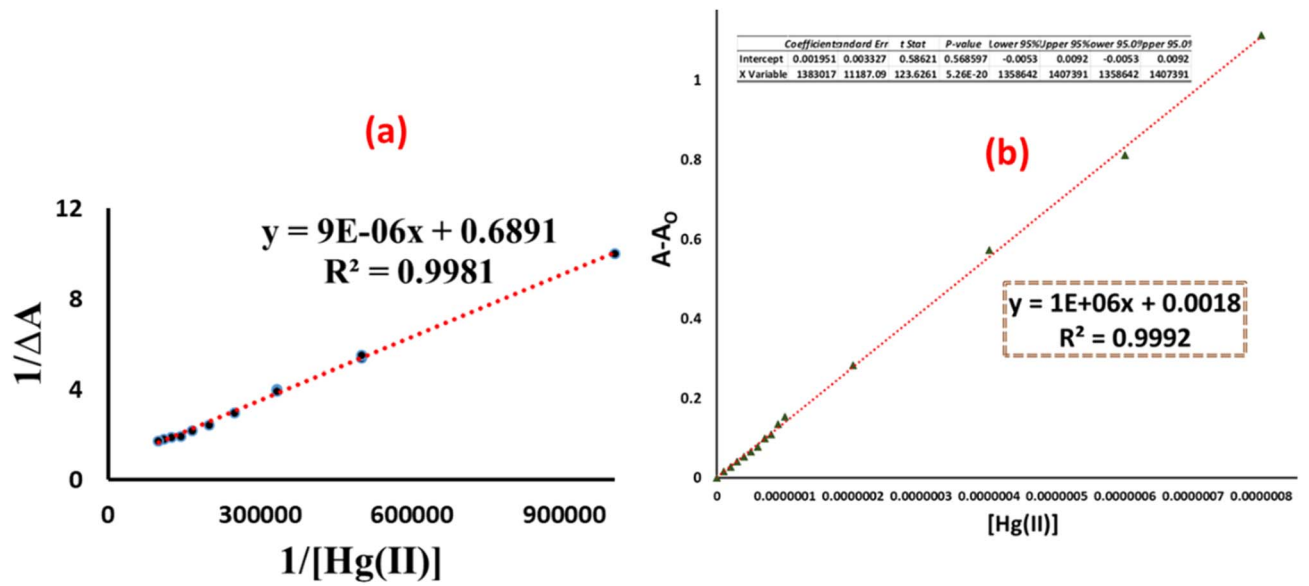

Fig. 5 (a) Benesi–Hildebrand plot for the stability constant of **TOMH** with Hg(II) from the absorbance data. (b) Calibration plot of **TOMH** with Hg(II) in a HEPES buffer (pH 7.4, containing 10% DMSO as a co-solvent).

experiments involving water were performed using UV-Vis spectroscopy in DMSO solvent spanning water fractions from 0% to 90% (Fig. 2a). The appearance of a new peak at 372 nm across the water fraction range indicated the formation of a new species, probably **TOMHN** (Fig. 3a). After reaching 90% water content, the absorbance sharply decreases, ruling out the formation of the **TOMHN** complex beyond this level. Thus, it is concluded that the sensor properties of **TOMH** are operative in a DMSO medium with water tolerance from 0% to 90%.

In the next phase, the effect of pH changes on the sensitivity of the **TOMH** sensor was examined in the pH range 2–12 using UV-visible spectroscopy (Fig. 2b) (the pH of the medium was altered using HCl or NaOH). The analysis of the pH-induced changes of the diagnostic 372 nm band, presumably of **TOMHN** complex, showed that **TOMH** was pH-insensitive between 2.07 and 10.30. In contrast, there was a notable increase in **TOMHN** intensity at pH 4.05, and thereafter the intensity remained relatively stable until pH 11.03.

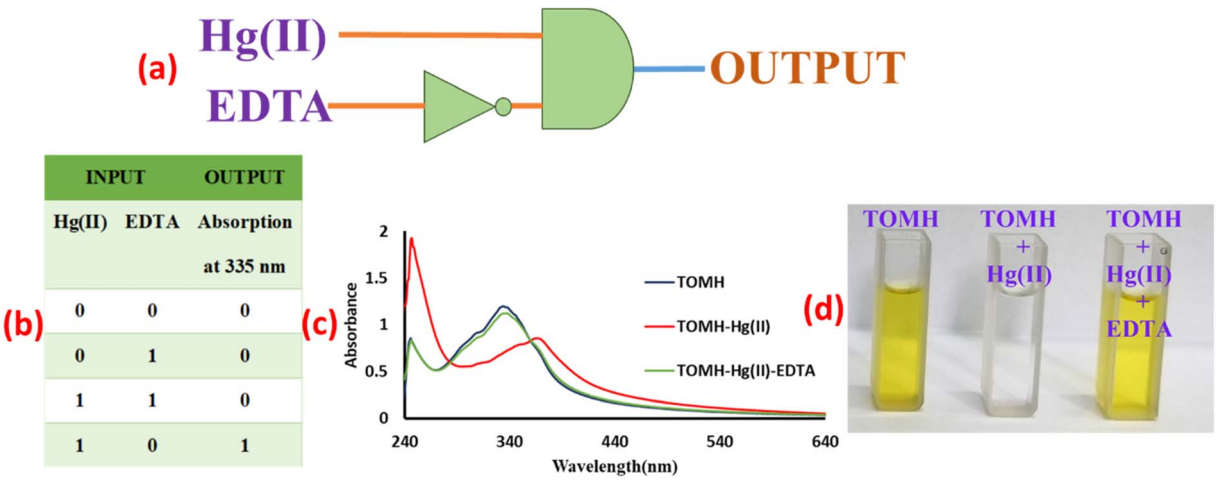

INPUT		OUTPUT
Hg(II)	EDTA	Absorption at 335 nm
0	0	0
0	1	0
1	1	0
1	0	1

Fig. 6 (a) Schematic of an INHIBIT logic gate and (b) truth table. (c) UV-vis spectra and (d) visual color outputs of **TOMH** with Hg(II) and EDTA solutions.

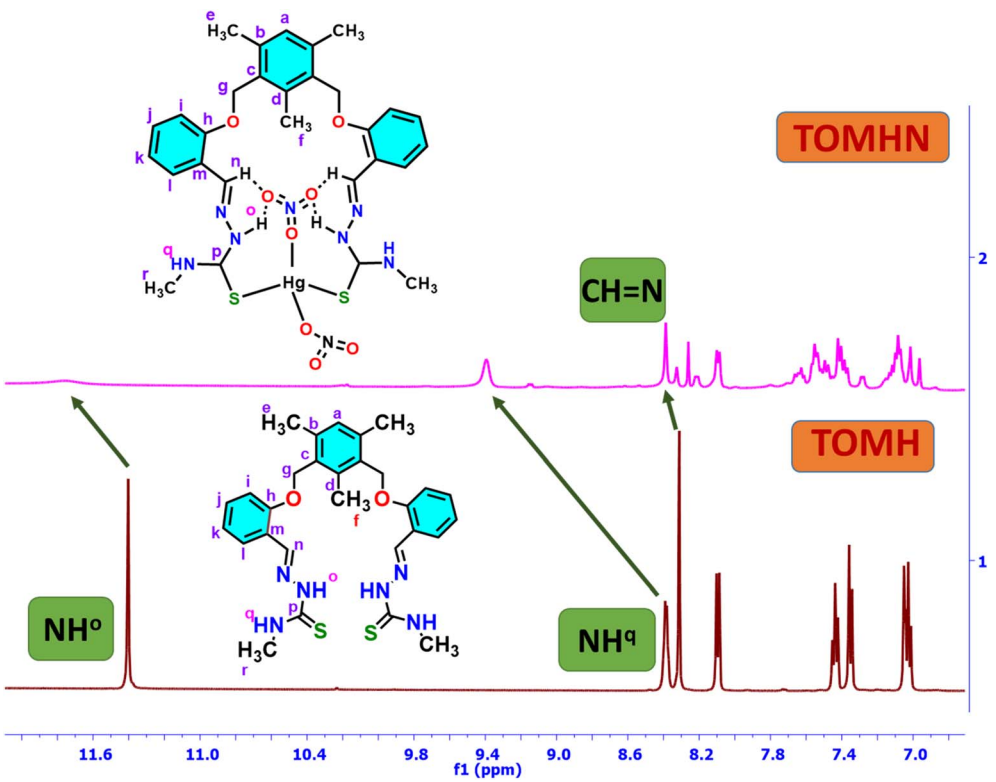

Fig. 7 Overlay of the partial ^{1}H NMR spectra of **TOMH** and **TOMHN** in DMSO-d_6 (range: δ 12.2–δ 6.9 ppm).

Significantly, this is the accepted range for studies of several biological systems. Therefore, the water content was maintained at 90% in the DMSO–water solvent system at pH 7.4 (DMSO : H_2O, 1 : 9, v/v) throughout the experiment.

The electronic absorption spectrum of **TOMH** in HEPES buffer (pH 7.4, containing 10% DMSO as a co-solvent) exhibits three absorption bands, centred at λ_{max} = 246 nm (ε_{max} = 81 800 M^{-1} cm^{-1}) assigned to a $\pi \rightarrow \pi^*$ electronic transition; λ_{max} = 305 nm (ε_{max} = 94 100 M^{-1} cm^{-1}) due to $n \rightarrow \pi^*$ (–C=N–) transition, and λ_{max} = 335 nm (ε_{max} = 124 500 M^{-1} cm^{-1}) ascribed to another $n \rightarrow \pi^*$ (–C=S–) transition[89,90] (Fig. S16). With the gradual addition of Hg(II), the electronic environment of **TOMH** changed, thereby altering its optical properties. The high-energy band at λ_{max} 246 nm increased in intensity, with the appearance of an isobestic point at 358 nm and a new band at λ_{max} 372 nm (ε_{max} = 88 200 M^{-1} cm^{-1}) (Fig. 3a). The appearance of an isobestic point supported the formation of a 1 : 1 complex, $Hg(NO_3)_2$(TOMH). This optical density change was accompanied by a color change from yellow to colorless (Fig. 3b).

Further, screening of **TOMH** with various metal ions under study, such as Al(III), Ag(I), Ba(II), Bi(III), Ca(II), Cd(II), Co(II), Cr(III), Cs(I), Cu(II), Fe(III), K(I), Li(I), Mg(II), Mn(II), Na(I), Ni(II), Pb(II), Th(IV), and Zr(IV), did not show any visible effect. However, there was a small effect with Zn(II), indicating a weak interaction, as it belongs to the same d^{10} group (Fig. 4a). **TOMH** reliably detects Hg(II) ions without interference from other metal ions, as demonstrated by tests in which 100 μM solutions of various metal ions under study were added to a mixture of 10 μM **TOMH** and 50 μM Hg(II) which showed no significant spectral changes (Fig. S17). A Job's plot[91] determined the stoichiometry of the interaction of Hg(II) with **TOMH.** For solutions with mole fractions from 0.1 to 0.9 of Hg(II), the absorption values are shown in Fig. 4b. From this curve, it can be seen that, at the highest absorbance, the mole fraction is 0.5, which suggests the formation of a 1 : 1 complex, namely, $Hg(NO_3)_2$(TOMH).

The Benesi–Hildebrand plot,[92] obtained by titrating **TOMH** with Hg(II), was used to calculate the binding constant, which was 7.65 × 10^4 M^{-1} (Fig. 5a). The limit of detection (LOD) of the **TOMH** sensor, which indicates its sensitivity, was calculated

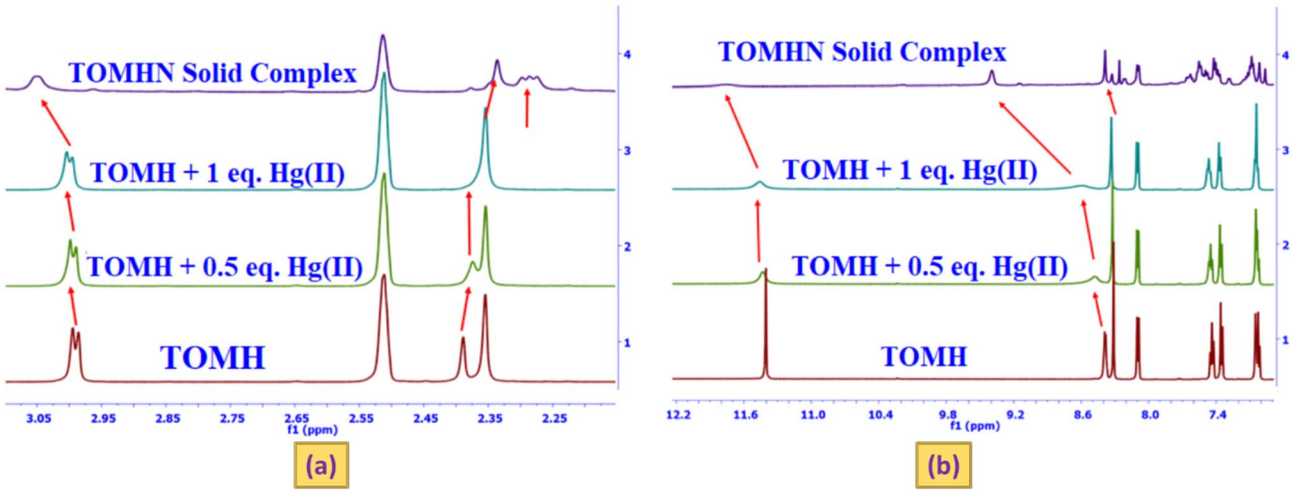

Fig. 8 Overlay of the partial ^{1}H NMR spectra of **TOMH** (5 mM) with increasing amounts of $Hg(NO_3)_2$ and the solid **TOMHN** complex in the ranges of (a) δ 3.10–δ 2.25 ppm and (b) δ 12.2–δ 6.9 ppm.

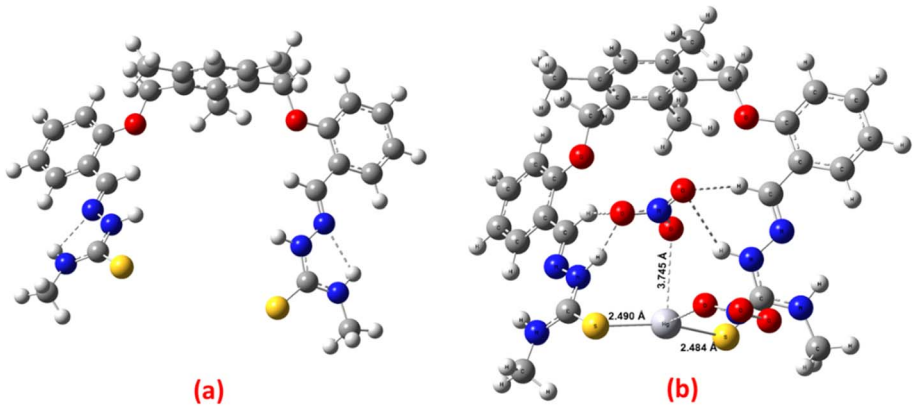

Fig. 9 3D optimized geometries of (a) **TOMH** and (b) **TOMHN**.

from the standard deviation (σ) of absorbance in the **TOMH** solution without analyte, followed by titrations with varying Hg(II) concentrations (Fig. 5b). Using the formula $3\sigma/k$, where k is the slope of absorbance *vs.* concentration, the LOD was determined. The World Health Organisation (WHO, 2011) states that drinking water typically contains about 0.001 mg L^{-1} of mercury.[93] Interestingly, **TOMH** can detect Hg levels as low as 0.01097 μM (10.97 nM), which is less than the WHO maximum permissible level.

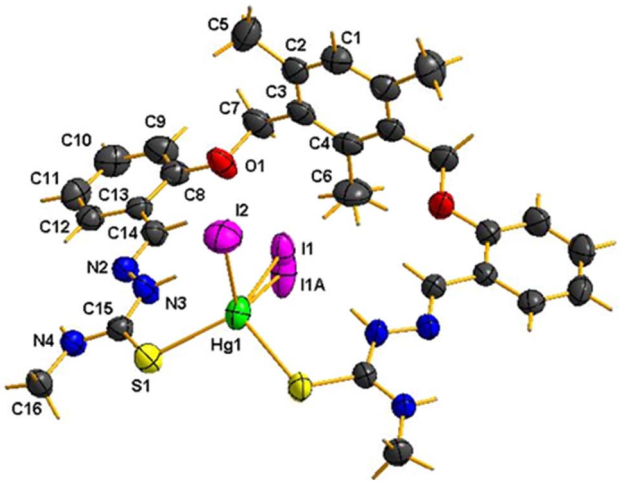

Fig. 10 ORTEP diagram of the TOMHI complex drawn in 25% thermal probability ellipsoids showing the atomic numbering scheme. The solvent acetonitrile has been removed for clarity.

To demonstrate reversibility, a 1 : 10 mixture of **TOMH** and Hg(II) was titrated with 100 μM EDTA, showing increased absorbance at 335 nm upon EDTA addition, indicating **TOMH** regeneration (Fig. 6). This reproducibility was further confirmed by reintroducing Hg(II) ions. Investigations into logic gates[94] confirmed **TOMH**'s reversible chromogenic response, enabling the construction of an INHIBIT logic gate with two inputs: EDTA and Hg(II) ion. An "OFF" or "0" state occurs when both inputs are absent or when only EDTA is present. An "ON" or "1" state occurs with a notable decrease in absorbance at 335 nm when only Hg(II) is introduced, which is consistent with the INHIBIT logic gate architecture. For environmental testing, **TOMH** demonstrated strong selectivity for Hg(II), as indicated by colorimetric analysis, which is corroborated by a solid-state study of filter paper strips. This experiment shows a color change (Fig. S18) from yellow to nearly colorless upon interaction with aqueous Hg(II). The strips demonstrated excellent stability, showing no color change even after two weeks.

3.2. Spectroscopic, structural, and computational studies

In order to further understand the interaction of the **TOMH** sensor with Hg(II) ions, NMR titrations were performed in DMSO-d_6 (Fig. 7, 8, and S19). The hydrazinic (=N–NH^o–) and thioamide protons {–NH^q–C(=S)–} of free **TOMH** appeared at δ 11.42 and δ 8.40 ppm and shifted to the low field region at δ 11.76 and δ 9.39 ppm, respectively. This result clearly supported the coordination of **TOMH** to Hg(II) ion through S donor atoms (Fig. 7). Signals for other protons of **TOMH**, namely –CH=N group (δ 8.30 ppm) and methyl protons {(CH_3)–NH^q–C(=S)–} (δ 2.99 ppm), showed small low field shifts to δ 8.39

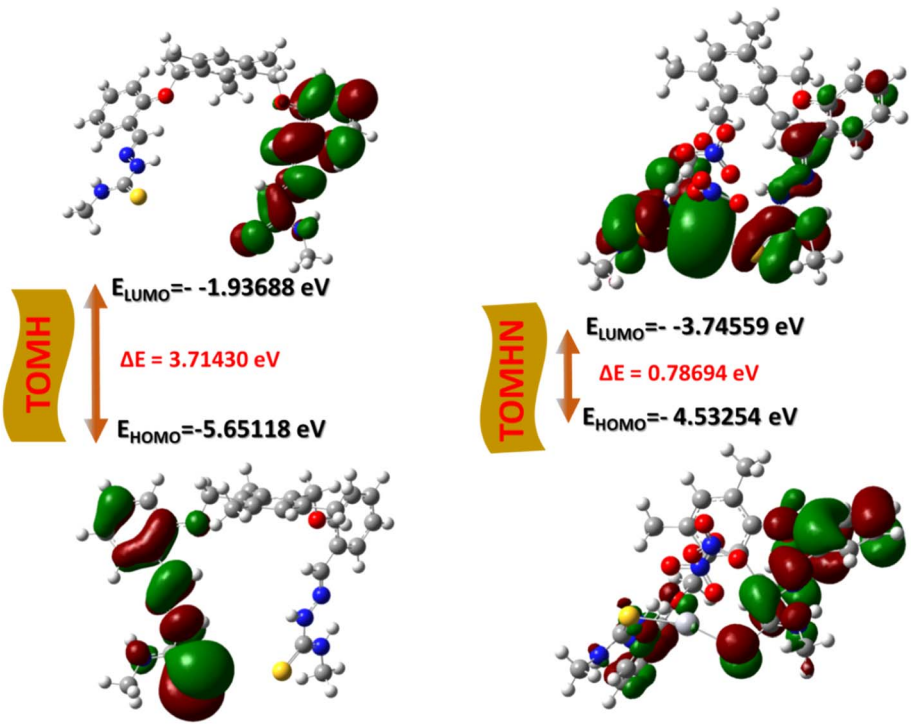

Fig. 11 HOMOs and LUMOs of TOMH and its nitrate complex TOMHN.

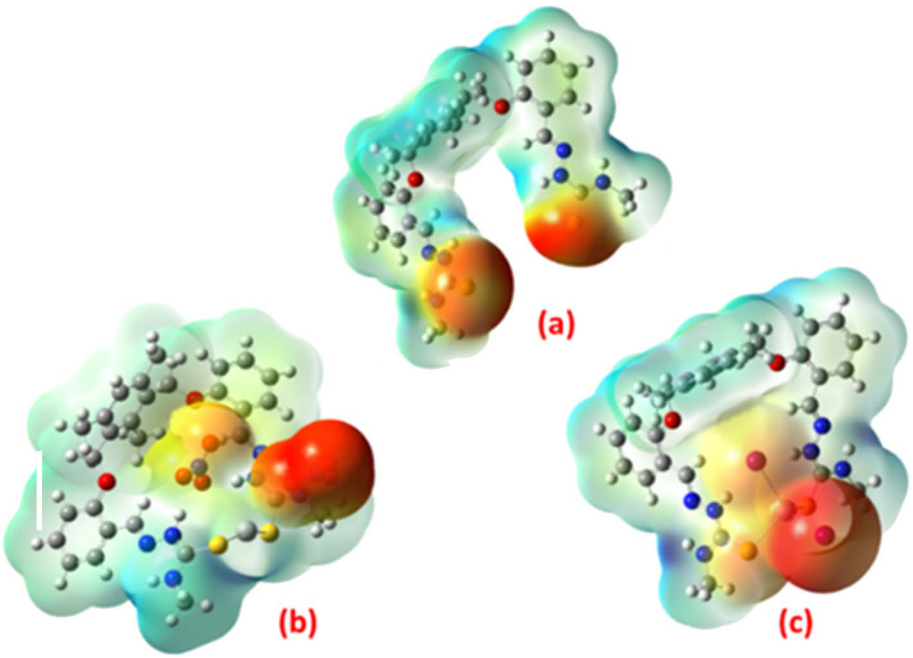

Fig. 12 ESP diagrams of (a) **TOMH**, (b) **TOMHN** complex, and (c) **TOMHI** complex (the red region indicates an electron-rich site, and the light blue region indicates an electron-deficient site).

and 3.05 ppm when **TOMH** binds to Hg(II). The methyl protons on the mesitylene ring appear as two distinct signals, in both the **TOMH** and **TOMHN** complex, with a 2 : 1 intensity ratio. The single methyl group (C6) of the **TOMHN** complex shifts upfield, from δ 2.39 ppm to δ 2.28 ppm, compared to the other two methyl groups (C5 at δ 2.36 ppm). This upfield shift of the C(6) protons probably results from the diamagnetic effect of the neighbouring mesitylene ring in the complex (Fig. 8a). The aromatic protons in the range of δ 8.13–δ 7.00 ppm also shift downfield, while the methylene protons remain almost unchanged (Fig. 8b). In the ^{13}C NMR of **TOMH**, the –C=S peak at δ 177.77 ppm shifted to δ 173.04 in the **TOMHN** complex (Fig. S19). Both the ^{1}H and ^{13}C NMR data very clearly support the coordination of **TOMH** to Hg forming the complex Hg(S,S-TOMH)$\cdot(NO_3)_2$.

The significant IR spectral bands (Fig. S20) of the **TOMHN** complex and **TOMH** are listed in Table S2. The interaction of mercury with **TOMH** affects several bands. In the **TOMH**-mercury nitrate complex, *viz.* **TOMHN**, the coordination of Hg to two sulfur functional moieties of **TOMH** shifts the diagnostic ν(C=S) band from 1082 cm^{-1} to 1026 cm^{-1}. Additionally, other groups, such as ν(N–H) and ν(C–H), which fall in the vicinity of the HgS_2 coordination core are also affected. The hydrazinic ν(N–H) stretching mode (=N–NH^{o}–) of **TOMH** around 3329 cm^{-1} shifts to a lower energy, appearing at 3202 cm^{-1} in **TOMHN**. Similarly, the ν(C–H) bands shift to lower energy in the **TOMHN** complex. The appearance of an IR band due to ν(N–O) at 1300 cm^{-1} suggests the ionic character of the complex Hg(TOMH)$\cdot(NO_3)_2$. Other bands, including ν(C=N), δ(N–H), ν(C–N), δ(C–H), and ν(C–O), appear at different positions in the **TOMHN** complex compared to in the free ligand.

When establishing the formation of Hg–S and Hg–O bonds (if any from NO_3) in the **TOMHN** complex, the lack of single-crystal formation of Hg(TOMH)$(NO_3)_2$ due to the amorphous nature of mercury nitrate (Fig. S11) prevented an X-ray structural study. Nonetheless, a computational study of both the chemosensor **TOMH** and its nitrate complex, **TOMHN**, was conducted to understand the bonding modes of **TOMH** with mercury(II) nitrate. The 3D optimized geometry of **TOMH** is shown in Fig. 9a, while that of its nitrate complex, **TOMHN**, is shown in Fig. 9b. Although not coplanar, both thiosemicarbazone arms of **TOMH** are in *cis*-orientation, enabling effective metal binding.

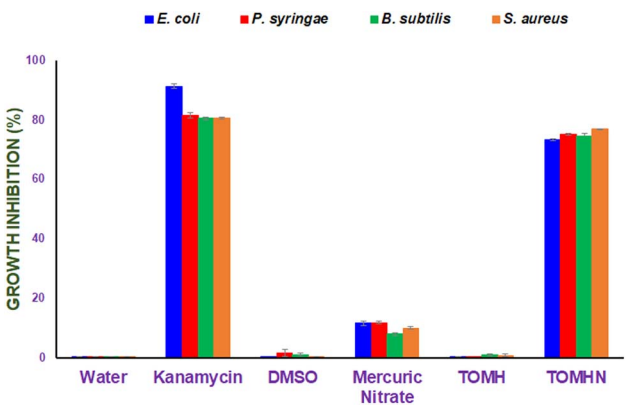

Fig. 13 Antimicrobial activity analysis of **TOMHN** against Gram-positive and Gram-negative bacteria. Bars represent mean ± SE (n = 3). Different letters (a, b, c, d, and e) represent values that were significantly different among different samples (Fisher LSD, $p \leq 0.05$).

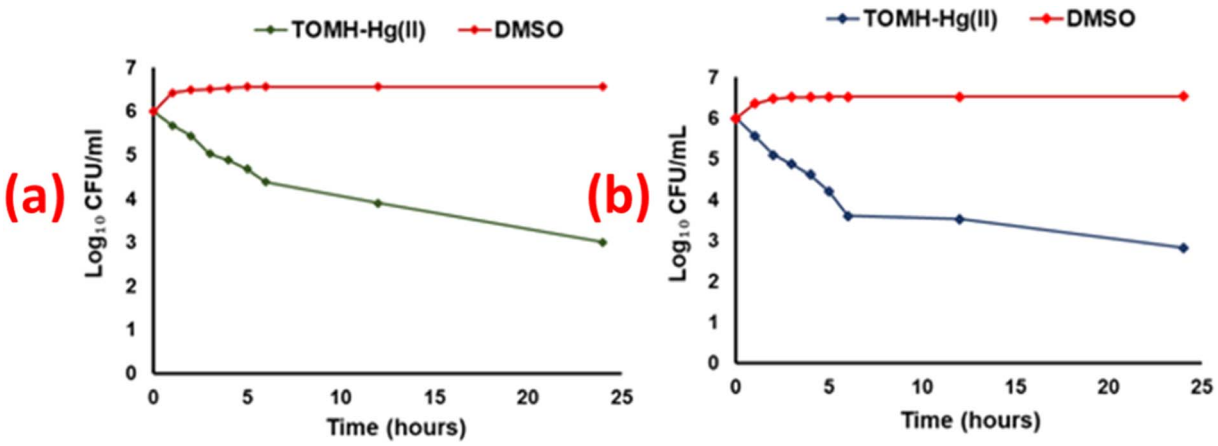

Fig. 14 Time-kill analysis of the TOMHN complex against (a) *E. coli* and (b) *S. aureus*.

The observed –C═S bond length of 1.676 Å indicates the nearly double-bond character of this moiety of **TOMH**. In the nitrate complex, **TOMHN**, mercury is bonded to two sulfur donor atoms with S–Hg bond lengths of 2.484–2.490 Å and an effective coordination number of two, with an S–Hg–S bond angle of 160.1°. The –C═S bond lengths in **TOMHN**, between 1.735 and 1.745 Å, are longer than in **TOMH**, suggesting a weakening of the pπ–pπ bonding of the –C═S groups when sulfur binds to Hg(II). Additionally, one $-NO_3$ group is near the –CH and –NH protons, participating in intermolecular H-bonding, which helps stabilize the nitrate complex (Fig. 9b, average O···H bond lengths ranging from 1.815 to 2.969 Å). The Hg···O (NO_3) bond distances, 3.439 Å and 3.767 Å, are beyond the sum of the van der Waals radii for Hg and O (3.00 Å),[95] indicating that uncoordinated nitrate ions remain close to Hg as H-bonded species (Fig. 9b).

The crystal structure of the related iodide complex, **TOMHI**, confirms Hg–S bond formation (Fig. 10 and S21–S23; see Table S3 for crystal parameters). Here, Hg binds to two sulfur atoms at equal distances of 2.5676(10) Å and to iodine atoms at distances of 2.7249(6) Å (Hg–I2), 2.854(5) Å (Hg1–I1), and 2.860(3) Å (Hg1–I1A). It is noted that I1 is spatially distorted, occupying positions I1 and I1A, and the minor difference in bond lengths is attributed to thermal distortion of the iodine atom. The complex exhibits a distorted tetrahedral geometry with bond angles between 101° and 115°. The S1–Hg1–S1 bond angle is 106.20(5)°, and the I2–Hg–I1 angle is 101.48(17)°, with the Hg–S bond distances being shorter in the nitrate complex than in the iodide one due to differences in coordination geometry. The Hg–S distance of 2.860 Å aligns with the sum of covalent radii for Hg and S. Hence, the strong Hg–S interaction in the nitrate complex is crucial for sensing Hg at nanomolar levels in aqueous media amidst various metal ions.

Finally, TD-DFT calculations were used to analyze the absorption spectra and charge-transfer properties of **TOMH**, **TOMHN**, and **TOMHI** (Fig. S24–S26). The HOMO–LUMO energy gap in **TOMH** is 3.71 eV, decreasing to 0.78 eV upon Hg(II) coordination in **TOMHN**, indicating energy release during binding (Fig. 11). The C═S bond lengths are 1.676 Å in **TOMH**, 1.735–1.745 Å in **TOMHN**, and 1.716 Å in **TOMHI**, positioned between typical single (1.81 Å) and double bonds (1.69 Å), confirming the partial double-bond character in the complexes. Molecular electrostatic potential surface (MESP) analysis[96,97] (Fig. 12) reveals strong sulfur-Hg(II) interactions, with **TOMH** showing electron-rich S centers and **TOMHN** indicating a more pronounced S–Hg(II)–S site.

3.3. Antimicrobial studies

Thiosemicarbazones and related compounds have a variety[98–104] of applications; mercury-based thiosemicarbazones exhibit antimicrobial properties.[105–114] In light of our research on the sensing properties of **TOMH** for Hg(II) ions, we were interested in studying the antimicrobial activity of **TOMH** and its nitrate complex, $Hg(NO_3)_2$(**TOMH**). Fig. 13 shows a plot of the growth inhibition percentages for both Gram-positive and Gram-negative bacteria. Kanamycin, used as a positive control, demonstrated the highest antibacterial activity against *E. coli*, *P. syringae*, *B. subtilis*, and *S. aureus*, with growth inhibition values exceeding 80%. As a negative control, DMSO showed very little inhibition. The sensor **TOMH** exhibited less than 1% growth inhibition, while $Hg(NO_3)_2$ displayed 8–12% bacterial growth inhibition. Interestingly, the nitrate complex, **TOMHN**, showed high antibacterial activity, ranging from 73.3% (*E. coli*) to 76.9% (*S. aureus*). The minimal inhibitory concentration (MIC) of **TOMHN** was determined to be 14.57 μM for *E. coli* and 12.85 μM for *S. aureus*, indicating effective antimicrobial activity at low concentrations.

The time-kill analysis revealed a progressive decline in antimicrobial activity when tested against *E. coli* and *S. aureus*. This suggested that the **TOMHN** complex exhibited bactericidal activity over time (Fig. 14).

4 Conclusion

In the present investigation, the **TOMH** chemosensor exhibits the lowest LOD for Hg ions (10.97 nM) in a water-rich medium among thiosemicarbazones or closely related S donor chemosensors (Table S1). It exhibits multiple application possibilities,

such as in on-site detection of Hg using filter paper strips, formation of an INHIBIT logic gate, and enhanced antimicrobial activity of **TOMHN** relative to that of **TOMH** or $Hg(NO_3)_2$ alone. In literature, mono-thiosemicarbazone and other related sulfur-containing chemosensors exhibited high LODs (21 nM to 69.02 μM) for Hg detection in a relatively organic solvent-rich medium of study. The sensing activity of **TOMH** remains unaffected in the pH range 2.07 to 10.30, supporting its working ability even in a biological medium. The low detection limit of **TOMH** may be attributed to both the *cis*-orientation of the sulfur-containing arms of the dipodal chemosensor and stronger S,S-chelation by **TOMH** to Hg ions, keeping in mind the HSAB principle.

Author contributions

Sanyog Sharma (conceptualization, experimentation, data analysis and manuscript drafting); Nabajyoti Patra (DFT studies and concerned data analysis); Navdeep Kaur (antimicrobial activity and concerned data analysis); Pratap Kumar Pati (antimicrobial data analysis, and supervision); Sanjay Mandal (X-ray data curation); P. V. Bharatam (DFT data curation, and supervision); and Tarlok Singh Lobana (conceptualization, review and editing). All authors have approved the final version of the manuscript.

Conflicts of interest

There are no conflicts to declare.

Data availability

CCDC 2470765 (**TOMHI**) contains the supplementary crystallographic data for this paper.[115]

Supplementary information (SI): spectral characterization of **TOMH**, **TOMHN**, and **TOMHI**; UV-vis responses; literature comparison; NMR titrations; IR analysis, crystal data and structure refinement for **TOMHI**; powder diffractogram; DFT studies of **TOMH**, **TOMHN**, and **TOMHI**. See DOI: https://doi.org/10.1039/d6ra02561g.

Acknowledgements

SS is grateful for the funding received under the DST-Women Scientist-A (WOS-A) program {DST/WOS-A/CS-64/2021} from the Department of Science and Technology (DST), Government of India. SS is also thankful to Dr Geeta Hundal for the crystal data analysis. Tarlok Singh Lobana thanks the National Academy of Sciences of India for the 'NASI Honorary Scientist Fellowship'. NK is thankful to the DST for the fellowship.

References

1 P. B. Tchounwou, C. G. Yedjou, A. K. Patlolla and D. J. Sutton, Molecular, Heavy metal toxicity and the environment, Clinical and, *Environ. Toxicol.*, 2012, **101**, 133–164.
2 T. W. Clarkson and L. Magos, The toxicology of mercury and its chemical compounds, *Crit. Rev. Toxicol.*, 2006, **36**, 609–662.
3 T. Rush, X. Liu and D. Lobner, Synergistic Toxicity of the Environmental Neurotoxins Methylmercury and β-Nmethylamino-L-alanine, *NeuroReport*, 2012, **23**, 216–219.
4 L. Amin-Zaki, S. Elhassani, M. A. Majeed, T. W. Clarkson, R. A. Doherty and M. Greenwood, Intra-uterine methylmercury poisoning in Iraq, *Pediatrics*, 1974, **54**, 587–595.
5 P. Jung-Duck and Z. J. Wei, Human Exposure and Health Effects of Inorganic and Elemental Mercury, *J. Prev. Med. Publ. Health*, 2012, **45**, 344–352.
6 L. Björkman, B. F. Lundekvam, T. Laegreid, B. I. Bertelsen, I. Morild and P. Lilleng, Mercury in human brain, blood, muscle and toenails in relation to exposure: An autopsy study, *Environ. Health*, 2007, **6**, 30.
7 M. T. Qamar, M. Aslam, I. M. Ismail, N. Salah and A. Hameed, Synthesis, characterization, and sunlight-mediated photocatalytic activity of CuO-coated ZnO for the removal of nitrophenols, *ACS Appl. Mater. Interfaces*, 2015, **7**, 8757–8769.
8 H. N. Kim, W. X. Ren, J. S. Kim and J. Yoon, Fluorescent and colorimetric sensors for detection of lead, cadmium, and mercury ions, *Chem. Soc. Rev.*, 2012, **41**, 3013–3432.
9 L. Liu, K. Ye, C. Lin, Z. Jia, T. Xue, A. Nie, Y. Cheng, J. Xiang, C. Mu, B. Wang, F. Wen, K. Zhai, Z. Zhao, Y. Gong, Z. Liu and Y. Tian, Grain-boundary-rich polycrystalline monolayer WS2 film for attomolar-level Hg(II) sensors, *Nat. Commun.*, 2021, **12**, 3870–3877.
10 R. D. Hancock, The pyridyl group in ligand design for selective metal ion complexation and sensing, *Chem. Soc. Rev.*, 2013, **42**, 1500–1524.
11 C. C. Bridges, B. F. Krasnikov, L. Joshee, J. T. Pinto, A. Hallen, J. Li, R. K. Zalups and A. J. L. Cooperb, New Insights into the Metabolism of Organomercury Compounds: Mercury-containing Cysteine S-conjugates are Substrates of Human Glutamine Transaminase K and Potent Inactivators of Cystathionine γ-lyase, *Arch. Biochem. Biophys.*, 2012, **517**, 20–29.
12 R. K. B. Barvin, P. Prakash, V. Ganesh and B. Jeyaprabha, Highly Selective and Sensitive Sensing of Toxic Mercury Ions Utilizing Carbon Quantum Dot-Modifed Glassy Carbon Electrode, *Int. J. Environ. Res.*, 2019, **13**, 1015–1023.
13 D. B. Liu, W. S. Qu, W. W. Chen, W. Zhang, Z. Wang and X. Y. Jiang, Highly sensitive, colorimetric detection of mercury(II) in aqueous media by quaternary ammonium group-capped gold nanoparticles at room temperature, *Anal. Chem.*, 2010, **82**, 9606–9610.
14 Y. Xu, L. Deng, H. Wang, X. Ouyang, J. Zheng, J. Li and R. Yang, Metal-induced aggregation of mononucleotides-stabilized gold nanoparticles: An efficient approach for simple and rapid colorimetric detection of Hg (II), *Chem. Commun.*, 2011, **47**, 6039–6041.
15 J. Wu, L. Li, D. Zhu, P. He, Y. Fang and G. Cheng, Nanomaterial-based optical sensors for mercury ions, *Anal. Chim. Acta*, 2011, **694**, 115–119.

16 WHO, *Guidelines for Drinking-Water Quality*, WHO, Geneva, 4th edn, 2011.
17 EPA, *EPA's Drinking Water Regulations for Mercury*, EPA 816-F09-004, EPA, Washington, DC, 2009.
18 C. T. Driscoll, R. P. Mason, H. M. Chan, D. J. Jacob and N. Pirrone, Mercury as a Global Pollutant: Sources, Pathways, and Effects, *Environ. Sci. Technol.*, 2013, **43**, 4967–4983.
19 K. Bontoom, M. Boonkitpatarakul and N. Sukwattanasinitt, Niamnont, Selective detection of Cu^{2+} based on a thiosemicarbazone triphenylacetylene fluorophore, *Tetrahedron Lett.*, 2017, **73**, 2483–2487.
20 N. S. Lakshmi, S. Young-Kyo and B. Sung-Ok, Speciation and determination of mercury by various analytical techniques, *Rev. Anal. Chem.*, 2013, **32**, 225–245.
21 N. Pourreza and R. Hoveizavi, Simultaneous Preconcentration of Cu, Fe and Pb as Methylthymol Blue Complexes on Naphthalene Adsorbent and Flame Atomic Absorption Determination, *Anal. Chim. Acta*, 2005, **549**, 124–128.
22 W.-S. Zhong, T. Ren and L.-J. Zhao, Determination of Lead, Cadmium, Chromium, Copper and Nickel in Chinese Tea with High Resolution Continuum Source Graphite Furnace Atomic Absorption Spectrometry, *J. Food Drug Anal.*, 2016, **24**, 46–55.
23 M. Behbahani, Y. Bide, M. Salarian, M. Niknezhad, S. Bagheri, A. Bagheri and M. R. Nabid, The Use of Tetragonal Star-like Polyaniline Nanostructures for Efficient Solid Phase Extraction and Trace Detection of Pb(II) and Cu(II) in Agricultural Products, Sea Foods and Water Samples, *Food Chem.*, 2014, **158**, 14–19.
24 A. M. Amlani and Z. R. Turel, Substoichiometric Determination of Copper by Neutron-Activation Analysis, *J. Radioanal. Nucl. Chem. Lett.*, 1990, **144**, 27–33.
25 K. E. Daugherty, R. J. Robinson and J. I. Mueller, X-Ray Fluorescence Spectrometric Determination of the Copper(II) and Mercury(II) Complexes of 6-Chloro-2-Methoxy-9- Thiolacridine, *Anal. Chem.*, 1964, **36**, 1098–1100.
26 Z. Yan, M.-F. Yuen, L. Hu, P. Suna and C.-S. Lee, Advances for the colorimetric detection of Hg^{2+} in aqueous solution, *RSC Adv.*, 2014, **4**, 48373–48388.
27 S. P. Kollur, C. Shivamallu, S. K. Prasad, R. Veerapur, S. S. Patil, C. A. Cull, J. F. Coetzee and R. G. Amachawadi, Recent Advances on the Development of Chemosensors for the Detection of Mercury Toxicity: A Review, *Separations*, 2021, **8**, 192–208.
28 U. Salma, M. Z. Alam, S. Ahmad, M. Mohasin and S. A. Khan, Recent Progress in Triazole Based Chromogenic and Fluorogenic Chemosensor for the Detection of Hg^{2+} Metal ion: A Review, *J. Fluoresc.*, 2025, **35**, 10201–10231.
29 S. Chakraborty, K. Das and S. Halder, A review on chemo sensors and fluro sensors of mercury ions, *Inorg. Chim. Acta*, 2024, **566**, 122026–122037.
30 D. Udhayakumari, Fluorescent and Colorimetric Methods for Mercury Sensing: Trends and Applications, *J. Fluoresc.*, 2025, **35**, 10763–10781.
31 B. Liu, J. Zhuang and G. Wei, Recent advances in the design of colorimetric sensors for environmental monitoring, *Environ. Sci. Nano*, 2020, **7**, 2195–2213.
32 M. A. Tarighat, F. H. Ghorghosheh and G. Abdi, Fe3O4@SiO2-Ag nanocomposite colorimetric sensor for determination of arginine and ascorbic acid based on synthesized small size AgNPs by cystoseria algae extract, *Mater. Sci. Eng., B*, 2022, **283**, 115855–115863.
33 S. H. Cho, J. M. Suh, T. H. Eom, T. Kim and H. W. Janh, Colorimetric Sensors for Toxic and Hazardous Gas Detection: A Review, Electron, *Mater. Lett.*, 2021, **17**, 1–17.
34 Q. Lin, Y. P. Fu, P. Chen, T. B. Wei and Y. M. Zhang, Colorimetric chemosensors designed to provide high sensitivity for Hg^{2+} in aqueous solutions, *Dyes Pigm.*, 2013, **96**, 1–6.
35 D. Udhayakumari, Fluorescent and Colorimetric Methods for Mercury Sensing: Trends and Applications, *J. Fluoresc.*, 2025, **35**, 10763–10781.
36 S. Sharma, M. S. Hundal, N. Singh and G. Hundal, Nanomolar fluorogenic recognition of Cu(II) in aqueous medium-A highly selective "on−off" probe based on mesitylene derivative, *Sens. Actuators, B*, 2013, **188**, 590–596.
37 S. Sharma, M. S. Hundal, A. Walia, V. Vanita and G. Hundal, Nanomolar fluorogenic detection of Al(III) by a series of Schiff bases in an aqueous system and their application in cell imaging, *Org. Biomol. Chem.*, 2014, **12**, 4445–4453.
38 S. Sharma, G. Dubey, B. S. Sran, P. V. Bhartam and G. Hundal, Fabrication of a Hydrazone-Based Al(III)-Selective "Turn-On" Fluorescent Chemosensor and Ensuing Potential Recognition of Picric Acid, *ACS Omega*, 2019, **4**, 18520–18529.
39 S. Sharma, M. S. Hundal and G. Hundal, Dual channel chromo/fluorogenic chemosensors for cyanide and fluoride ions – an example of in situ acid catalysis of the Strecker reaction for cyanide ion chemodosimetry, *Org. Biomol. Chem.*, 2013, **11**, 654–661.
40 S. Sharma, J. Singh, N. Singh and G. Hundal, Spectroscopic and theoretical evaluation of solvent-assisted, cyanide selectivity of chromogenic sensors grounded on mesitylene platform and their biological applications, *Sens. Actuators, B*, 2016, **225**, 141–150.
41 S. Sharma, B. S. Sran, N. Singh and G. Hundal, From Dual to Discriminatory Sensing of CN-/F- Using Isomeric Molecules and Ascertained by Spectroscopic and DFT Methods, *ChemistrySelect*, 2018, **3**, 3225–3233.
42 S. Sharma, M. S. Hundal and G. Hundal, Selective recognition of fluoride ions through fluorimetric and colorimetric response of a first mesitylene based dipodal sensor employing thiosemicarbazones, *Tetrahedron Lett.*, 2013, **54**, 2423–2427.
43 S. Sharma, G. Dubey, B. S. Sran, M. Sharma, V. Kaur, S. Kaur, P. V. Bharatam and G. Hundal, Microwave-Induced Synthesis of Pyridine-Based Schiff Bases and their applications as efficient antimicrobial textile dyeing agents: Experimental and theoretical approach, *ChemistrySelect*, 2022, **7**, e202203109.

44 V. K. Bhardwaj, S. Sharma, N. Singh, M. S. Hundal and G. Hundal, New tripodal and dipodal colorimetric sensors for anions based on tris/bis-urea/thiourea moieties, *Supramol. Chem.*, 2011, **23**, 790–800.
45 O. Özbek and C. C. Berkel, Sensor properties of thiosemicarbazones in different analytical methods, *Polyhedron*, 2023, **238**, 116426–116442.
46 S. Khanna, Analysis of thiosemicarbazones as an effective spectrophotometric chemosensor, *Phosphorus, Sulfur Silicon Relat. Elem.*, 2025, **200**, 37–45.
47 M. L. F. Jardim, M. M. M. Raposo and S. P. G. Costa, A Novel Heterocyclic Thiosemicarbazone: Synthesis, Characterization and Preliminary Sensing Studies for Ions, *Chem. Proc.*, 2021, **8**, 53.
48 J. H. Ajudiya and M. C. Shah, Thiosemicarbazones Are Good Spectrophotometric Reagent for Transition Metal Determination: A Review, *YMER*, 2022, **21**, 152–175.
49 R. K. Mahajan, I. Kaur and T. S. Lobana, A mercury (II) ion-selective electrode based on neutral salicylaldehyde thiosemicarbazone, *Talanta*, 2003, **59**, 101–105.
50 L. Feng, W. Shi, J. Ma, Y. Chen, F. Kui, Y. Hui and Z. Xie, A novel thiosemicarbazone Schiff base derivative with aggregation-induced emission enhancement characteristics and its application in Hg^{2+} detection, *Sens. Actuators, B*, 2016, **237**, 563–569.
51 Y. Li, W. Shi, J. Ma, X. Wang, X. Kong, Y. Zhang, L. Feng, Y. Hui and Z. Xie, A novel optical probe for Hg^{2+} in aqueous media based on mono-thiosemicarbazone Schiff base, *J. Photochem. Photobiol., A*, 2017, **338**, 1–7.
52 Z. E. Chen, H. Zhang and Z. Iqbal, A new thiosemicarbazone fluorescent probe based on 9, 9′ -bianthracene for Hg^{2+} and Ag^{+}, *Spectrochim. Acta, Part A*, 2019, **215**, 34–40.
53 T. Wei, J. Li, C. Bai, Q. Lin, H. Yao, Y. Xie and Y. Zhang, A highly selective colorimetric sensor for Hg^{2+} based on a copper (II) complex of thiosemicarbazone in aqueous solutions, *Sci. China: Chem.*, 2013, **56**, 923–927.
54 K. Ghosh and D. Tarafdar, A new quinolone-based chemosensor in ratiometric sensing of Hg^{2+} ions, *Supramol. Chem.*, 2013, **25**, 127–132.
55 X. Li, K. Du, C. Xie, Y. Wu, B. Zhang and D. Tang, A Highly Sensitive and Selective Colorimetric Probe Based on a Cycloruthenated Complex: An Hg^{2+}-Promoted Switch of Thiophene Coordination, *Dalton Trans.*, 2020, **49**, 2024–2032.
56 Y. Wu, X. Cheng, C. Xie, K. Du, X. Li and D. Tang, A Polymer Membrane Tethered with a Cycloruthenated Complex for Colorimetric Detection of Hg^{2+} Ions, *Spectrochim. Acta*, 2020, **228**, 117541.
57 P. Karuppusamy, J. Senthilvelan, V. Vijayakumar and S. Sarveswari, A Pyrazole-Based Highly Selective Colorimetric Chemosensor for Hg^{2+} Ion in Semi-Aqueous Medium, *ChemistrySelect*, 2020, **5**, 49–53.
58 M. Z. Jonaghani and H. Zali-Boeini, Highly selective fluorescent and colorimetric chemosensor for detection of Hg^{2+} ion in aqueous media, *Spectrochim. Acta, Part A*, 2017, **178**, 66–70.
59 Z. Aydın, A Cinnamaldehyde-based Colorimetric Sensor for Hg^{2+} Detection in Aqueous Solutions, *J. Inst. Sci. Tech.*, 2021, **11**, 376–383.
60 E. Normaya, M. F. A. Hamdan, M. N. Ahmad, Y. F. A. Aziz and K. H. K. Bulat, DFT/TD-DFT study on development and optimization of 1-anilino-3-phenyliminourea as a colorimetric chemosensor for Hg^{2+} recognition in aqueous medium, *J. Mol. Struct.*, 2020, **1206**, 127699–127708.
61 H. Jeon, H. Ryu, I. Nam and D. Y. Noh, Heteroleptic Pt (II)-Dithiolene-Based Colorimetric Chemosensors: Selectivity Control for Hg (II) Ion Sensing, *Materials*, 2020, **13**, 1385.
62 M. B. I. Mohamed, M. S. El-Sedik, Y. A. Youssef, N. A. Mohamed and T. S. Aysha, New stilbene-biscarbothioamide based colorimetric chemosensor and turn on fluorescent probe for recognition of Hg^{2+} cation, *J. Photochem. Photobiol., A*, 2022, **433**, 114206–114218.
63 T. Anand and M. Sankar, A Dual Colorimetric Chemosensor for Hg (II) and Cyanide Ions in Aqueous Media Based on a Nitrobenzoxadiazole (NBD)–Antipyrine Conjugate with INHIBIT Logic Gate Behaviour, *Anal. Methods*, 2020, **12**, 4526–4533.
64 H. Hosseinjani-Pirdehi, N. O. Mahmoodi, M. P. Nadamani and A. Taheri, Novel Synthesized Azo-Benzylidene-Thiourea as Dual Naked-Eye Chemosensor for Selective Detection of Hg^{2+} and CN^{-} Ions, *J. Photochem. Photobiol.*, 2020, **391**, 112365.
65 F. Ye, X.-M. Liang, K.-X. Xu, X.-X. Pang, Q. Chai and Y. Fu, A novel dithiourea-appended naphthalimide "on-off" fluorescent probe for detecting Hg^{2+} and Ag^{+} and its application in cell imaging, *Talanta*, 2019, **200**, 494–502.
66 L. Qi, Y.-P. Fu, P. Chen, W. Tai-Bao and Y.-M. Zhang, Colorimetric chemosensors designed to provide high sensitivity for Hg^{2+} in aqueous solutions, *Dyes Pigm.*, 2013, **96**, 1–6.
67 Y.-X. Yang, W.-Y. Zhang, Y. Fan, X.-Q. Sun, R.-C. Li, C.-Y. Zhang, X.-X. Feng, N.-Z. Jin and J.-C. Liu, Porphyrin-based Schiff base fluorescent probe: Mercuric ion recognition by naked eye colorimetric analysis and application of test strip detection, *J. Mol. Struct.*, 2024, **1312**, 138506.
68 M. Tripathy, U. Subuddhi and S. Patel, An Azo Dye Based D-π-A Chromogenic Probe for Selective Naked-Eye Detection of Hg^{2+} Ion: Application in Logic Gate Operation, *ChemistrySelect*, 2020, **5**, 4803–4815.
69 S. Pattaweepaiboon, T. Nanok, N. Kaewchangwat, K. Suttisintong and W. Sirisaksoontorn, Colorimetric detection of Hg^{2+} and CH_3Hg^{+} by a novel spirooxazine derivative as a highly sensitive and selective probe, *Dyes Pigm.*, 2021, **186**, 108996–109005.
70 B. Kaur, A. Gupta and N. Kaur, A novel, anthracene-based naked eye probe for detecting Hg^{2+} ions in aqueous as well as solid state media, *Microchem. J.*, 2020, **153**, 104508.
71 S. Chakraborty, K. Das and S. Halder, A review on chemo sensors and fluro sensors of mercury ions, *Inorg. Chim. Acta*, 2024, **566**, 122026–122037.

72 A. W. van der Made and R. H. van der Made, A Convenient Procedure for Bromomethylation of Aromatic Compounds. Selective Mono-, Bis-, or Trisbromomethylation, *J. Org. Chem.*, 1993, **58**, 1262–1263.
73 O. V. Dolomanov, L. J. Bourhis, R. J. Gildea, J. A. K. Howard and H. Puschmann, OLEX2: A Complete Structure Solution, Refinement and Analysis Program, *J. Appl. Crystallogr.*, 2009, **42**, 339–341.
74 G. M. Sheldrick, SHELXT – Integrated space-group and crystal-structure determination, *Acta Crystallogr., Sect. A*, 2015, **71**(71), 3–8.
75 W. Kohn, A. D. Becke and R. G. Parr, Density Functional Theory of Electronic Structure, *J. Phys. Chem.*, 1996, **100**, 12974–12980.
76 J. B. Foresman, and A. E. Frisch, *Exploring Chemistry with Electronic Structure Methods*, Gaussian. Inc. Wallingford, CT USA. 2015.
77 P. W. Atkins, and R. S. Friedman, *Molecular Quantum Mechanics*. Oxford University Press, 2011.
78 M. J. Frisch, G. W. Trucks, H. B. Schlegel, G. E. Scuseria, M. A. Robb, J. R. Cheeseman, G. Scalmani, V. Barone, G. A. Petersson, H. Nakatsuji, X. Li, M. Caricato, A. V. Marenich, J. Bloino, B. G. Janesko, R. Gomperts, B. Mennucci, H. P. Hratchian, J. V. Ortiz, A. Izmaylov, F. Sonnenberg, J. L. Williams-Young, F. Ding, F. Lipparini, F. Egidi, J. Goings, B. Peng, A. Petrone, T. Henderson, D. Ranasinghe, V. G. Zakrzewski, J. Gao, N. Rega, G. Zheng, W. Liang, M. Hada, M. Ehara, K. Toyota, R. Fukuda, J. Hasegawa, M. Ishida, T. Nakajima, Y. Honda, O. Kitao, H. Nakai, T. Vreven, K. Throssell, J. A. Montgomery Jr, J. E. Peralta, F. Ogliaro, M. J. Bearpark, J. J. Heyd, E. N. Brothers, K. N. Kudin, V. N. Staroverov, T. A. Keith, R. Kobayashi, J. Normand, K. Raghavachari, A. P. Rendell, J. C. Burant, S. S. Iyengar, J. Tomasi, M. Cossi, J. M. Millam, M. Klene, C. Adamo, R. Cammi, J. W. Ochterski, R. L. Martin, K. Morokuma, O. Farkas, J. B. Foresman, and D. J. Fox, *Gaussian 16, Revision B.01*, Gaussian, Inc., Wallingford CT, 2016.
79 F. Weigend and R. Ahlrichs, Balanced basis sets of split valence, triple zeta valence and quadruple zeta valence quality for H to Rn: Design and assessment of accuracy, *Phys. Chem. Chem. Phys.*, 2005, **7**, 3297–3305.
80 J. F. Janak, Proof that $\delta E/\delta n_i = \varepsilon_i$ in density-functional theory, *Phys. Rev. B*, 1978, (12), 7165–7168.
81 R. G. Parr, L. V. Szentpàly and S. Liu, Electrophilicity Index, *J. Am. Chem. Soc.*, 1999, **121**, 1922–1924.
82 J. P. Perdew, Density-Functional Theory for Fractional Particle Number: Derivative Discontinuities of the Energy, *Phys. Rev. Lett.*, 1982, **49**, 1691–1694.
83 R. Parthasarathi, V. Subramanian, D. R. Roy and P. K. Chattaraj, Electrophilicity index as a possible descriptor of biological activity, *Bioorg. Med. Chem.*, 2004, **12**, 5533–5543.
84 N. Patra, A. Gupta and P. V. Bharatam, Stable, aromatic, and electrophilic azepinium ions: Design using quantum chemical methods, *J. Comput. Chem.*, 2024, **46**, e27520.
85 H. Kaur, M. Singh, N. Kaur, P. K. Pati, M. Rani and T. S. Kang, Sustainable dissolution of collagen and the formation of polypeptides in deep eutectic solvents for application as antibacterial agents, *RSC Sustainability*, 2024, **2**, 2312–2323.
86 C. Mellinas, M. Ramos, A. Grau-Atienza, A. Jordà, N. Burgos, A. Jiménez, E. Serrano and M. D. C. Garrigós, Biodegradable poly (ε-caprolactone) active films loaded with MSU-X mesoporous silica for the release of α-tocopherol, *Polymers*, 2020, **12**, 137–156.
87 M. Patel, M. S. Ashraf, A. J. Siddiqui, S. A. Ashraf, M. Sachidanandan, M. Snoussi, M. Adnan and S. Hadi, Profiling and role of bioactive molecules from puntius sophore (Freshwater/brackish fish) skin mucus with its potent antibacterial, antiadhesion, and antibiofilm activities, *Biomolecules*, 2020, **10**, 920–925.
88 S. Shanmugam and B. V. Pradeep, Studies on phytochemical screening and antibacterial activity of rhizome extracts of Coleus forskohlii Briq, *J. Pure Appl. Microbiol.*, 2019, **13**, 1703–1710.
89 D. Luneau and C. Evans, New Schiff base zinc(II) complexes exhibiting second harmonic generation, *J. Chem. Soc., Dalton Trans.*, 2002, 83–86.
90 A. Koll, Specific Features of Intramolecular Proton Transfer Reaction in Schiff Bases, *Int. J. Mol. Sci.*, 2003, **4**, 434–444.
91 P. Job, Formation and stability of inorganic complexes in solution, *Ann. Chim.*, 1928, **9**, 113–203.
92 H. Benesi and H. Hildebrand, A Spectrophotometric Investigation of the Interaction of Iodine with Aromatic Hydrocarbons, *J. Am. Chem. Soc.*, 1949, **71**, 2703–2707.
93 A. Shah, A. Arjunan, A. Baroutaji and J. Zakharova, A review of physicochemical and biological contaminants in drinking water and their impacts on human health, *Water Sci. Eng.*, 2023, **16**, 333–344.
94 L. Liu, P. Liu, L. Ga and J. Ai, Advances in Applications of Molecular Logic Gates, *ACS Omega*, 2021, **6**, 30189–30204.
95 J. E. Huheey, E. A. Keiter and R. L. Keiter, *Inorganic Chemistry: Principles of Structure and Reactivity*, Harper Collins, New York, 4th edn, 1993.
96 V. K. Dakua, A. Datta, D. Roy, D. Biswas, B. Ghosh, K. Roy, S. Paul, P. Das, S. Mishra and B. Sinha, Synthesis, crystal structure, Hirshfeld surface, and DFT studies of a Copper (II) complex of 5,5′-dimethyl-2,2′-bipyridine and 1,2,2-trimethylcyclopentane-1,3-dicarboxylic acid, *Results Chem.*, 2023, **6**, 101050–101057.
97 B. N. Socha, S. B. Pandya, B. R. Chavda, K. P. Chaudhary, T. J. Padariya, M. D. Alalawy, R. P. Dubey, U. H. Patel and R. H. Patel, Gas-phase DFT studies, quantum chemical calculation and 3D energy framework analysis of novel copper complex of sulfadimethoxine in the presence of secondary ligand 3-methyl pyridine, *Inorg. Nano-Metal Chem.*, 2021, **51**, 1822–1830.
98 T. S. Lobana, A. Sanchez, J. S. Casas, A. Castineiras, J. Sordo, M. S. Garcia-Tasende and E. M. Vazquez-Lopez, Symmetrisation, isomerism and structural studies on novel phenylmercury(II) thiosemicarbazonates: A correlation of energy barrier to rotation of amino group

with the bonding parameters of thioamide, *J. Chem. Soc., Dalton Trans.*, 1997, 4289–4299.

99 T. S. Lobana, Rekha, R. J. Butcher, A. Castineiras, E. Bermejo and P. V. Bharatam, Bonding trends of thiosemicarbazones in mononuclear and dinuclear copper(I) complexes: syntheses, structures and theoretical aspects, *Inorg. Chem.*, 2006, **45**, 1535–1542.

100 T. S. Lobana, R. Sharma and R. J. Butcher, Pyridine-2-thione (pySH) derivatives of silver(I): synthesis and crystal structures of dinuclear $[Ag_2X_2(\mu\text{-S-pySH})_2(PPh_3)_2]$ complexes (X = Cl, Br), *Polyhedron*, 2008, **27**, 1375–1380.

101 T. S. Lobana, G. Bawa, A. Castineiras and R. J. Butcher, Synthesis of Cu^{II}-Ru^{II}-Cu^{II} trinuclear complexes via redox reaction of copper(I) across thiosemicarbazones coordinated to ruthenium(II), *Inorg. Chem.*, 2008, **47**, 1488–1495.

102 F. M. Alkhatib, T. A. Farghaly, M. F. Harras and H. A. El-Ghamry, Copper(II) complexes based on 1,3,4-thiadiazolethiosemicarbazone NNS donor ligands: synthesis, molecular structure, DNA binding and *in silico* molecular docking approach, *Inorg. Nano-Metal Chem.*, 2024, **54**, 18–29.

103 K. M. Takroni, T. A. Farghaly, M. F. Harras and H. A. EI-Ghamry, Synthesis, structure elucidation, DNA binding and molecular docking studies of novel copper(II) complexes of two 1,3,4-thiadiazolethiosemicarbazone derivatives, *Appl. Organomet. Chem.*, 2020, **34**, 1–16.

104 A. Fawzy, T. A. Farghaly, H. A. El-Ghamry and T. M. Bawazeer, Investigation of the inhibition efficiencies of novel synthesized cobalt complexes of 1,3,4-thiadiazolethiosemicarbazone derivatives for the acidic corrosion of carbon steel, *J. Mol. Struct.*, 2020, **1203**, 127447.

105 L. N. Suvarapu, A. R. Somala, J. R. Koduru, S. O. Baek and V. R. A. Ammireddy, A Critical Review on Analytical and Biological Applications of Thio-and Phenylthiosemicarbazones, *Asian J. Chem.*, 2012, **24**, 1889–1898.

106 P. Lam, G.-L. Lu, K. Choi, Z. Lin, S. H. L. Kok, K. K. H. Lee, K. Lam, H. Li, R. Gambari, Z. X. Bian, W. Y. Wong and C. H. Chui, Antimicrobial and Toxicological Evaluations of Binuclear Mercury (II) Bis (Alkynyl)Complexes Containing Oligothiophenes and Bithiazoles, *RSC Adv.*, 2016, **6**, 16736–16744.

107 C. M. Taylor, J. Golding and A. M. Emond, Blood Mercury Levels and Fish Consumption in Pregnancy: Risks and Benefits for Birth Outcomes in a Prospective Observational Birth Cohort, *Int. J. Hyg. Environ. Health*, 2016, **219**, 513–520.

108 F. Maqsood, S. S. Al-Rawi, A. H. Ibrahim, F. Jamil, A. Zafar, M. A. Iqbal, U. S. Shoukat, M. Asad, S. U. Zia, F. Ahmad and M. Atif, Recent trends in medicinal applications of mercury based organometallic and coordination compounds, *Rev. Inorg. Chem.*, 2024, 1–22.

109 A. Aliabadi, E. Motieiyan, F. Hosseinabadi, M. Ghadermazi and S. Abdolmaleki, One-Pot Synthesis, Crystallographic Characterization, Evaluation as In Vitro Antibacterial and Cytotoxic Agents of Two Mercury (II) Complexes Containing Pyridine Dicarboxylic Acid Derivatives, *J. Mol. Struct.*, 2021, **1226**, 129405–129413.

110 S. Khani, M. Montazerzohori, R. Naghiha and S. Joohari, Nano Structured Mercury (II) Schiff Base Complexes of a N3-Tridentate Ligand as New Biological Active Agents, *Inorg. Chem. Res.*, 2020, **4**, 279–294.

111 Y.-S. Wu, A. I. Osman, M. Hosny, A. M. Elgarahy, A. S. Eltaweil, D. W. Rooney, Z. Chen, N. S. Rahim, M. Sekar, S. C. B. Gopinath, N. N. I. M. Rani, K. Batumalaie and P.-S. Yap, The Toxicity of Mercury and Its Chemical Compounds: Molecular Mechanisms and Environmental and Human Health Implications: A Comprehensive Review, *ACS Omega*, 2024, **9**, 5100–5126.

112 S. J. Sabounchei, M. Ahmadianpoor, A. Hashemi, F. Mohsenzadeh and R. W. Gable, Synthesis, Spectroscopic and Structural Characterization and Antibacterial Activity of New Dimeric and Polymeric Mercury (II) Complexes of Phosphonium Ylide, *Inorg. Chim. Acta*, 2017, **458**, 77–83.

113 A. K. TG, V. Tekuria, M. Mohanb and D. R. Trivedia, Selective colorimetric chemosensor for the detection of Hg^{2+} and arsenite ions using Isatin based Schiff's bases; DFT Studies and Applications in test strips, *Sens. Actuators, B*, 2019, **284**, 271–280.

114 A. Chakraborty, V. K. Rajana, C. Saritha, A. Srivastava, D. Mandal and N. Das, A new Eosin Y-based 'turn single bond on' fluorescent sensor for ratiometric sensing of toxic mercury ion (Hg^{2+}) offering unaided eye detection and its antibacterial activity, *J. Hazard. Mater.*, 2024, **470**, 134207–134221.

115 CCDC 2470765: Experimental Crystal Structure Determination, 2026, DOI: 10.5517/ccdc.csd.cc2ny13s.